Journal of Oceanology and Limnology
Vol. 39 No. 1, P. 45-55, 2021
https://doi.org/10.1007/s00343-020-9346-8

Observation of continental shelf wave propagating along the eastern Taiwan Strait during Typhoon Meranti 2016*

Junqiang SHEN[1, 2, 3, **], Shanwu ZHANG[2], Junpeng ZHANG[2], Mingzhang ZENG[2], Wendong FANG[1]

[1] *State Key Laboratory of Tropical Oceanography, South China Sea Institute of Oceanology, Chinese Academy of Sciences, Guangzhou 510301, China*

[2] *Third Institute of Oceanography, Ministry of Natural Resources, Xiamen 361005, China*

[3] *University of Chinese Academy of Sciences, Beijing 100049, China*

Received Jan. 7, 2020; accepted in principle Feb. 29, 2020; accepted for publication Mar. 26, 2020

Abstract This study is the first to depict typhoon-induced continental shelf wave (CSW) propagation in the eastern Taiwan Strait (TWS) during the passage of Typhoon Meranti in 2016 using tidal gauge data and along-track satellite altimeter data. The strong amplitude response of sea level oscillations (within the range of 0.30–0.54 m) as a free, barotropic CSW after Meranti, which impacted the TWS, was clearly detected in time and frequency (in bands of 64–81 h) using wavelet and cross-wavelet analyses. The measured group and phase speeds were consistent with the dispersion curves for CSW with the first-mode derived from the cross-shelf sections of the eastern TWS, with the mean speeds reaching 3 and 5.6±0.7 m/s, respectively. Coincidentally, the typhoon-induced sea level anomaly (SLA) was also captured by the satellite altimeter before this CSW entered into the TWS. Using the theoretical cross-shore CSW modes to fit the SLA data, the results indicated that the first three wave modes can interpret this CSW event appeared in the southern TWS very well, with the first mode being the dominant one.

Keyword: continental shelf wave (CSW); tidal gauge data; satellite altimeter data; typhoon; Taiwan Strait

1 INTRODUCTION

The response characteristics of the upper ocean to moving typhoons are dynamically intricate (Price, 1981; Sanford et al., 1987), and the physical processes are highly complex in shallow waters (Schulz et al., 2012). Simple-form Kelvin waves and barotropic continental shelf waves (CSWs) can be generated accordingly after large-scale typhoon events; these waves can move along or cross continental shelf within a mid-latitude (Han et al., 2012; Chen et al., 2014). Several observational and modeling studies on the responses of coastal shallow waters to passing typhoons (Tang et al., 1998; Thiebaut and Vennell, 2010; Shen et al., 2017), showed that free CSWs could be generated.

The Taiwan Strait (TWS) is located between the South China Sea and the East China Sea (Fig.1), which is about 180-km wide, 350-km long, and on average 60-m deep (Chung et al., 2001). From April to November, the area suffers from frequent typhoons generated in the western Pacific Ocean. Due to lack of field observations under passing typhoons, the ocean response to typhoon forcing in the shallow water of the TWS is not well understood. Based on our knowledge, during a moving typhoon event, model simulations mainly focus on the issue of the barotropic waves propagating along the coast of the East China Sea and the South China Sea (Ding et al., 2011, 2012). In contrast, the TWS is treated as a transition area for those CSW events. In fact, the terrain of the TWS is very complex, especially the width of continental shelf is gradually reduced from the southern end to

* Supported by the Science Foundation of Fujian Province (No. 2019J01119), the Scientific Research Foundation of Third Institute of Oceanography, MNR (Nos. 2017011, 2019018), the National Natural Science Foundation of China (No. 41506014), and the National Key Research and Development Program of China (No. 2016YFC1402607)
** Corresponding author: jqshen@tio.org.cn

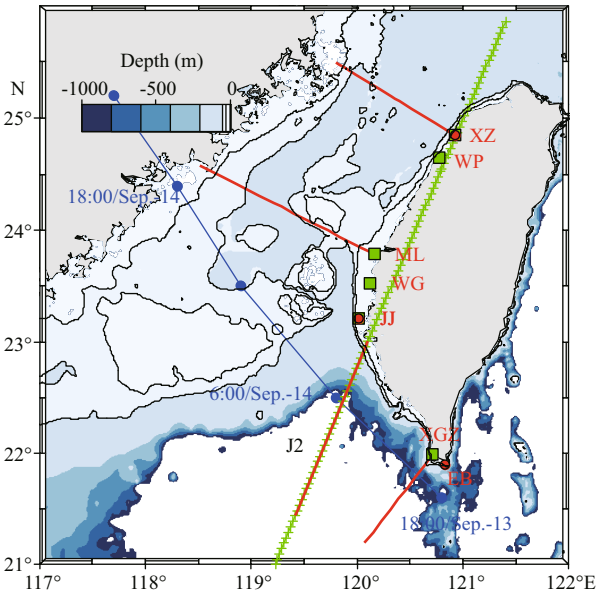

Fig.1 Map of the study area of the TWS and its adjacent seas

The track and locations of Typhoon Meranti at specifc times are shown as blue line with solid circles, which are obtained from the Regional Specialized Meteorological Center of Japan (http://www.jma.go.jp/jma/index.html). The green line with small crosses is the Jason-2 satellite ground track. Six tide-gauge stations and three meteorological buoys are depicted by green squares and red cycles, respectively. The red lines off the coast of Taiwan, China, indicate the cross-shelf transects where the dispersion relationship for the CSW is calculated. Since part of the Jason-2 satellite ground track is nearly perpendicular to the continental shelf; it was chosen to be one of the cross-shelf transects and labeled as J2. Major geographic locations labeled are Eluanbi Buoy (EB), Xunguanzui (XGZ), Jianjun (JJ), Wengang (WG), Miaoli (ML), Wangpin (WP), and Xinzu (XZ).

the interior of the strait, which will directly affect the propagation speed of the CSWs. Shen et al. (2017) presented direct measurements of free, barotropic CSWs propagating in the western TWS during the passage of Typhoon Saomai which transited from the north of the TWS. In another scenario, if the typhoon transits from the south of the TWS, will the CSWs be generated and propagate along the coast of the eastern TWS? If this hypothesis proves true, to identify the CSW events, the variation of the group and phase speeds of the typhoon-induced CSWs in this sea area, and the dominant spatial modal structure need further investigation. However, so far, this kind of CSW events has not been reported in this region. In addition, among a few similar events ever documented, it is the first time to combine the satellite altimetry with tide-gauge data to investigate CSW features in the TWS that could represent a typical case in this regard.

Meranti, a classic typhoon in the western Pacific, made landfall on mainland China at 18:00 UTC 14 September 2016 from the south of the TWS (Fig.1). It was the most severe typhoon in 2016 to hit the mainland and caused enormous damage to properties. In this study we will focus on this typhoon, which affected the TWS on 13 September 2016 and generated significant sea level oscillations (SLOs) propagating along the eastern coast of the TWS. Coincidently, the Jason-2 satellite altimeter flew over the Taiwan, China, shortly before the landfall of Meranti. Here, we combine this satellite altimetry with tide-gauge data to investigate the features of CWS propagating along the coast of the TWS.

The remainder of this study is organized as follows. In Section 2, the data sets and methodology are introduced. In Section 3, the alongshore and cross-shore characteristics of the CSW derived from the tidal gauge data and satellite altimeter along-track data are presented. In Section 4, a summary is drawn, and we further discuss the accuracy of the altimeter data which account for quantitatively diagnosing of the CSW event.

2 DATA AND METHOD

2.1 Overview of datasets

Tidal gauge data at six coastal stations on the east side the TWS (Fig.1) are obtained from the website of the Central Weather Bureau of Taiwan, Taiwan (China) (http://www.cwb.gov.tw). The data cover a period of September 5–25, 2016, with a temporal resolution of 1 h. De-tiding software (Pawlowicz et al., 2002) is used to remove the tidal component with the tidal gauge data (corrected by atmospheric pressure). Then, de-tided sea level anomaly (DSLA) is derived by removing their mean sea level and extracted the longwave records by low-pass filtering with a cutoff frequency of 1.41 cpd.

The along-track sea level anomaly (SLA) data are acquired and reprocessed by the Archiving, Validation and Interpretation of Satellite Oceanographic Data (AVISO), Center National d'Etudes Spatiales (CNES) of France (www.aviso.altimetry.fr). The corrections for ionosphere and tides, while multi-mission cross-calibration, have been applied to the data. In the study region, the data is distinguished with a temporal resolution of 1 s, and the spatial resolution of about 5.9 km. In addition, gridded monthly SLA data are also used as the background field in this study. The resolution of the gridded SLA data is about 0.25°×0.25°, with global ocean coverage.

In-situ wind speed was observed by three

meteorological buoys, of which the data with a time interval of 1 h from September 10–15, 2016, were used to depict the wind field during the passage of Meranti. As in situ meteorological data set is limited for the study area, we resorted to the hourly ERA-5 reanalysis wind stress field in a spatial resolution of 0.25°×0.25° (https://cds.climate.copernicus.eu). The information of the typhoon Meranti is obtained from the Regional Specialized Meteorological Center of Japan (http://www.jma.go.jp/jma).

2.2 Methodology

2.2.1 Wavelet transform

Wavelet transform is used to analyze time series data containing nonstationary power at different frequencies (Torrence and Compo, 1998). Because the time series of DSLA is nonstationary, with a large range of frequencies, especially during a typhoon event, a wavelet analysis, useful for extracting both time and frequency information from a time series is employed.

The continuous wavelet transform is defined as the convolution of the time series X_n with the scaled and normalized wavelet

$$w_n^X(s)=\sqrt{\delta_t/s}\sum_n^{N-1}x_n x\varphi\left[(n'-n)\delta_t/s\right], \quad (1)$$

where s is the wavelet scale, δ_t is the uniform time spacing, φ is the mother wavelet (or Morlet wavelet in this case), and n=0, 1, ⋯, N (N is the number of the points). In practice, the confidence interval for true wavelet power $W_n^2(s)$ is defined as

$$v\chi_v^{-2}(p/2)\left|W_n^X(s)\right|^2 \le w_n^{X^2}(s)\le v\chi_v^{-2}(1-p/2)\left|W_n^X(s)\right|^2, \quad (2)$$

where p is the desired significance, v is equal to 1 for real and 2 for complex wavelet, and $\chi_v^2(p/2)$ represents the value of χ_v^2 at $p/2$.

2.2.2 Cross-wavelet transform

The cross-wavelet transform (XWT) of two signals reveals the regions in both time and frequency space with high common power and exposes information of phase relationship (Grinsted et al., 2004). The CSW phase speed is estimated by calculating the XWT of pairs of stations. The XWT of two-time series X_n and Y_n is described as $W^{XY}=W^X W^{Y*}$, where W^X is the continuous wavelet transform of X_n, and their complex conjugate denoted with asterisk. The cross-wavelet power is further defined as $|W^{XY}|$. The phase relationship between X and Y in a time-frequency space is illustrated as the complex argument of W^{XY}.

To calculate the mean phase between two-time series, the circular mean of the phase over regions is used, which is higher than 5% statistical significance and within the given range of period. Lastly, a set of angles with the circular mean (a_i, i=1, ⋯, n) is proposed by Zar (1999),

$$a_m=\arg(X, Y), \quad (3)$$

with $X=\sum_{i=1}^n\cos(a_i)$ and $Y=\sum_{i=1}^n\sin(a_i)$. To estimate the confidence interval of the phase difference, we use the circular standard deviation defined as $S=\sqrt{-2In(R/n)}$, where $R=\sqrt{X^2+Y^2}$ (Grinsted et al., 2004).

2.2.3 CSW mode analysis

The dispersion relation for CSW in an idealized depth profile is given in Pedlosky (1987):

$$J_0\left(2\mu^{\frac{1}{2}}\right)\left[1-\left(F^{\frac{1}{2}}+F\right)\frac{\omega}{k}\right]= -\gamma\left(1-\frac{F}{\gamma}\frac{\omega}{k}\right)J_2\left(2\mu^{\frac{1}{2}}\right), \quad (4)$$

where J_0 and J_2 are the zero and second orders of the first kind of Bessel function, k is the wavenumber, ω is the wave frequency, γ is the ratio of the maximum shelf depth to the deep ocean depth. Herein, $\mu=\frac{klf}{\omega}-\frac{F}{\gamma}$ and $F=\frac{f^2l^2}{gD}$, where l is the continental shelf width, f is the Coriolis parameter, D is the deep ocean depth, and g is the gravitational acceleration.

As it is well known, in a CSW event, the CSW signal should be a prominent component. And the other signals are thought to be the background signals. Then, sea level signal observed by the satellite altimeter can be decomposed into an infinite number of CSW modes and the background signal $\varepsilon(\xi)$. We use $J_0(2\mu^{1/2}\xi^{1/2})$ to analyze the cross-shore characteristics of CSW on the shelf of the TWS, with the first three CSW modes in the form of

$$\eta=\begin{cases}\sum_{i=1}^3 A_i J_0\left(2\mu^{\frac{1}{2}}\xi^{\frac{1}{2}}\right)+\varepsilon' & \xi\le 1\\ \sum_{i=1}^3 A_i J_0\left(2\mu^{\frac{1}{2}}\xi^{\frac{1}{2}}\right)\exp\left(-F^{\frac{1}{2}}(\xi-1)\right)+\varepsilon' & \xi>1\end{cases}, \quad (5)$$

where $\xi=\chi/l$ is normalized cross-shore coordinate, and η is the sea level, A_i is the amplitude of each CSW mode, ε' is the remainder of ε after removing the signal with periods longer than a specified period, and in our case it is set to be one month. Such evaluations have been used for studies of the winter storm-induced CSWs in the northern South China Sea (Li et al., 2016).

3 RESULT

3.1 SLOs propagating along the coast

As shown in Fig.2a, large fluctuations of the SLOs within the range of 0.30–0.54 m can be observed at the coast after the passage of Meranti, suggesting that the response was mainly barotropic (Thiebaut and Vennell, 2010). Figure 2b shows the power density spectra of the DSLA derived from the fast Fourier transform using a Hanning window. One can see that the spectra at the six stations have a common period band of peaks, and all peaked at the center of 80.3 h (above the 95% statistical significance level) which represented the dominant period of the SLOs.

Interestingly, the SLOs propagate along the eastern coast of the TWS with obviously northward time lags (Fig.2a). Since the typhoon transits from the south, the observed northward time lags might indicate local responses that reflect the typhoon's northwest path. Note that, Meranti is the most intense typhoon of the western pacific in 2016, characterized by a minimum central pressure of 890 hPa and a maximum wind speed of 60 m/s. However, owing to the small radius (a maximum radius of 380 km), it cannot directly affect the entire TWS. Furthermore, we analyzed the in-situ wind speed data from three meteorological buoys during the passage of Meranti. As shown in Fig.2c, the further north station XZ reach the peak wind first, followed by the station EB (in the southern region), while JJ (in the middle of the strait) was the last station to reach the peak wind. Hence, it is believed that the SLOs do not mainly arise from local forcing. If so, they would not appear as gradual time lags from south to north among those stations since the synchronous wind field is not changing progressively from south to north. The observed propagating SLOs are therefore speculated to be the free CSW, which will be confirmed in Section 3.2.

Gordon and Huthnance (1987) and Tang et al. (1998) both pointed out that the ocean responses are closely related to the duration of atmospheric forcing. Power density spectra of the amplitude of sea surface wind stress (with the same period of DSLA), as shown in Fig.2d, contain peaks at periods of 24, 41, and 75 h, all above the 95% statistical significance level. Note that the period of 75 h is the only common peak for all stations, indicating the duration of the typhoon impacting the TWS. Next, we will find out that after Meranti passed over XGZ, the predominant period of CSW was limited in the resonant propagating regime (i.e., 64–81 h) for the other five stations (Fig.3a) and the center frequency (0.33 cpd) of this propagating CSW would be associated with the duration for the Meranti passing over the shelf, which is agreed with the CSW theory. The passing time of strong typhoon like Meranti is the key element that determines the propagation and the frequency band preferentially excited for the free CSW.

Because the above time series of the DSLA have a large range of period band during the passage of Meranti (Fig.2b), a wavelet analysis is employed to extract the information of common periods from the time series of DSLA. With the measurement of the distance between each pair of stations, the group speed of barotropic CSW is calculated by approximating the time of the maximum wavelet energy at each station. Such an evaluation method has been used previously for exploring the Yanai waves in the Atlantic Ocean (Meyers, 1993) and the dispersive waves in solid systems (Kishimoto et al., 1995; Park and Kim, 2001).

As shown in Fig.3a, the significant regions on wavelet power spectrum become narrower in period as one goes farther away from XGZ where the response includes periods from 28 to 94 h, which is due to the weakly dispersive effect of the lower-frequency waves with high group velocity and smaller wavenumber. In particular, the six wavelet power spectrums show a poleward propagation of a (64–81)-h period wave along the coast, after Meranti hit the TWS (Fig.3a). The maximum of each scale-averaged wavelet power (Fig.3b) gives a good approximation of the maximum amplitude of the barotropic CSW envelope. Table 1 shows the values used to calculate the barotropic CSW group speed along the coast after the passage of Meranti. Obviously, the group speed was large at the south entrance of the TWS, which could reach a speed of 8.5 m/s, but reduced to only 2–3 m/s in the TWS. It was related to the fact that the shelf width is reduced remarkably from the southern to the northern part of the TWS. This is consisting with the work of Jordi et al.(2005) which indicated that the fast-propagating wave could only exist over a wide continental shelf. The mean group speed was about 3.0 m/s during this CSW event, according to Table 1.

Furthermore, we calculate the XWT for pairs of the DSLA time series at different sites to obtain the phase speed of the CSW induced by Meranti. For instance, the results of these computations for adjacent station pairs are shown in Fig.4. One can easily see that in most cases, the former would lead the latter; however, the station pair of WG and ML in Fig.4c appears to be the opposite. Noteworthy, for the XWT (Table 2) of

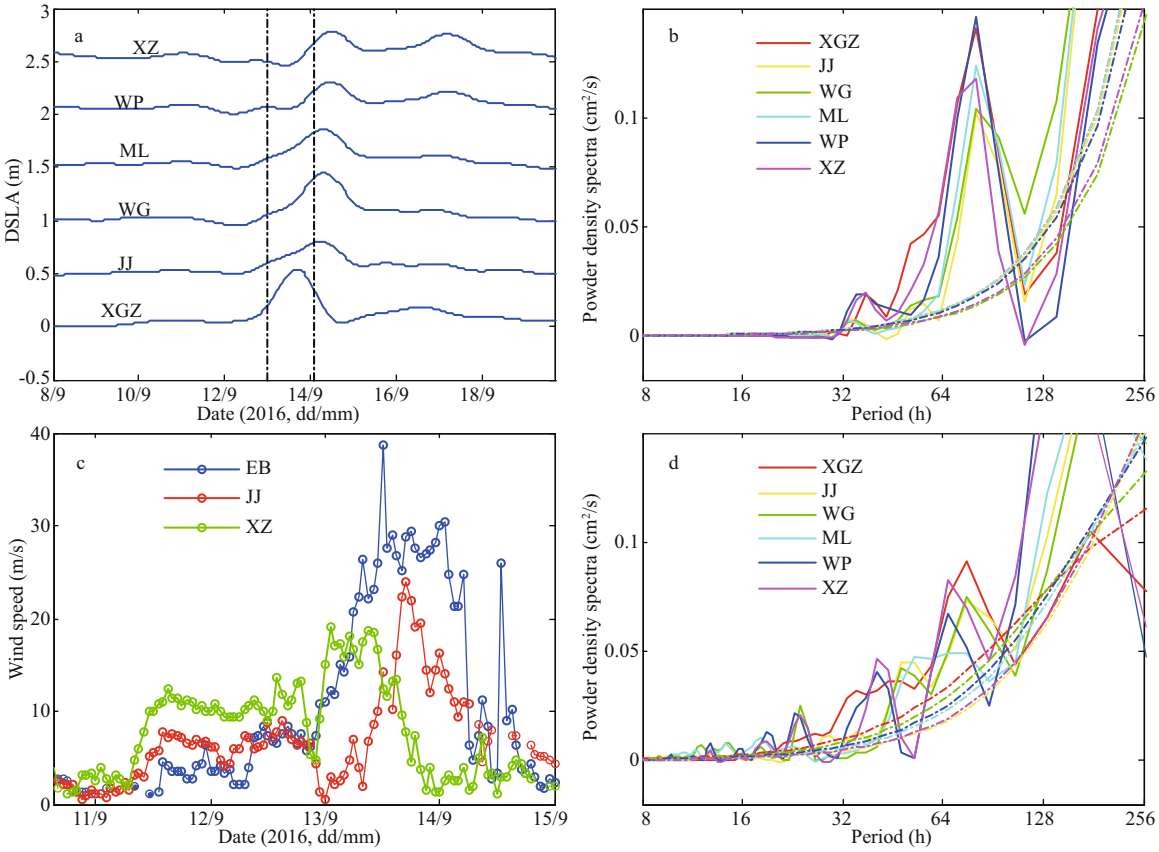

Fig.2 Time series of the atmospheric pressure-corrected DSLA (low-pass filtered with a cutoff frequency of 1.41 cpd) at the six tidal gauge stations (a) and in-situ observed wind speed at the three meteorological buoys (c); power density spectra of the DSLA (b) and amplitude of the wind stress at sea surface (d) at each station

Dotted vertical lines indicate the time when Meranti (front and back of the storm) hit the east coast of Taiwan, China. DSLA at each station is plotted with a shift of 0.5 m from 0 m in the *Y*-axis. The colored dashed lines represent the 95% confidence level.

WG with other stations, the magnitude of the CSW phase speed appears significantly larger (i.e., WG-ML\WP\XZ) or smaller (i.e., JJ-WG) than the other station pairs, and at the same time the former case would lead to a large variability. In addition, among those stations locate in TWS, the largest DSLA is also found at WG when the CSW transit the TWS. Given these, we speculate that the wave at station WG was forced wave directly affected by the local typhoon forcing. However, limited to the observation data, the explanation is not conclusive; the specific mechanism may be confirmed by further model work. We conclude that all station pairs, excluding WG, can be used to calculate the mean phase speed of the free CSW, and the mean phase speed of the CSW is then estimated to about 5.6 m/s with a mean error of 0.7 m/s.

3.2 Dispersion relation

The dispersion relation of shelf waves was determined by the given topographic shelf profile. In this study, we use the codes (with 2007 version)

Table 1 The concern values used for calculating the group speed (c_g) of CSW after the transit of typhoon Meranti

Station pair	Separation (km)	Lag (h)	Group speed (m/s)
XGZ-JJ	153.8	5	8.5
XGZ-WG	189.5	10	5.3
XGZ-ML	219.3	17	3.6
XGZ-WP	333.4	29	3.2
XGZ-XZ	360.0	32	3.1
JJ-WG	35.7	5	2.0
JJ-ML	65.5	12	1.5
JJ-WP	179.6	24	2.1
JJ-XZ	206.2	27	2.1
WG-ML	29.7	7	1.2
WG-WP	143.9	19	2.1
WG-XZ	170.4	22	2.2
ML-WP	114.2	12	2.6
ML-XZ	140.7	15	2.6
WP-XZ	26.5	3	2.5

The lag with a positive value indicates the second station of the pair would lead the first one. The positive component of c_g indicates that the energy propagating with the coastline on its right side.

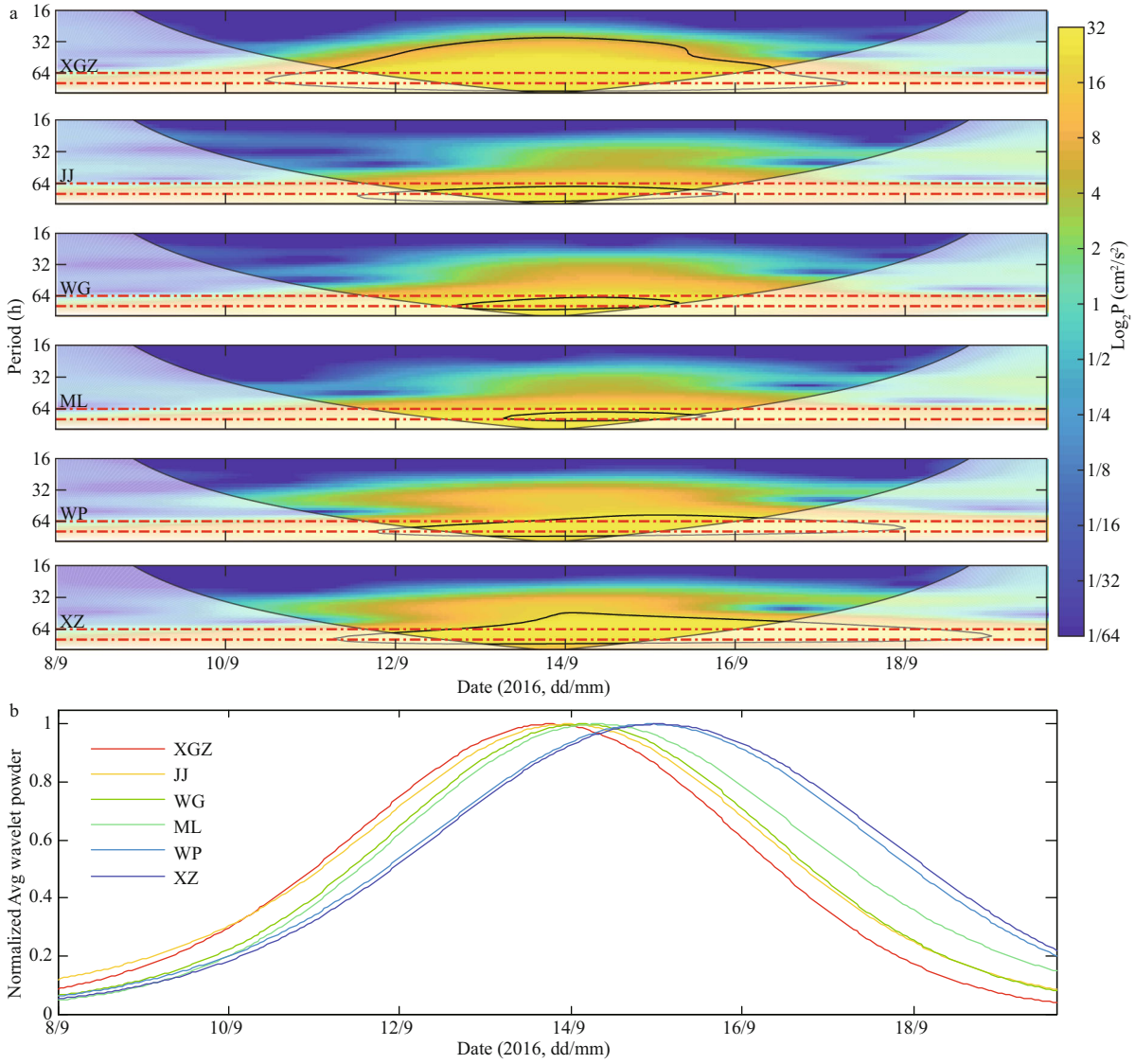

Fig.3 Morlet wavelet power spectrum of the DSLA at the six tide-gauge stations (a) (the thick line is the 5% significance level against red noise); scale-averaged wavelet power time series over the (64–81)-h band (denoted by the red dash lines in panel a for each station) at the six tide-gauge stations (b)

written by Brink and Chapman (1985) to derive the dispersion curves of barotropic CSW using four cross-shelf sections deployed along the eastern coast of the TWS (Fig.1). For a long shelf wave within the frequency band of around 0.33±0.03 cpd, the group speed estimated from the dispersion curves (Fig.5a) is within the range of 1.2–8.4 m/s, and the phase speed is estimated between 1.4 and 8.9 m/s (Fig.5b) given the shelf profiles at the four selected sections. The mean group and phase speeds calculated using wavelet and cross-wavelet analyses are up to 3 and 5.6±0.7 m/s, respectively, which are consistent with the theoretical estimates. The calculated results illustrate that the data points of SLOs distribute near the corresponding theoretical curves (Fig.5b), indicating they were mainly the barotropic CSWs propagating freely as the first mode.

3.3 Cross-shore sea level structure

The Jason-2 satellite altimetry flew over Taiwan, China, shortly before the landfall of Typhoon Meranti, and captured the storm surge off Taiwan, China. As a complement to tide-gauge observation, Jason-2 altimetry provides reliable information of storm surge magnitude and cross-shelf surge structure. As shown in Fig.6, the SLA increased sharply from the shelf edge at around 500-m isobath toward the coast, resulting in a large cross-shelf slope. The storm surge magnitude at the location close to the coast (about 11 km) was around 0.23–0.27 m (Fig.6b). At the time

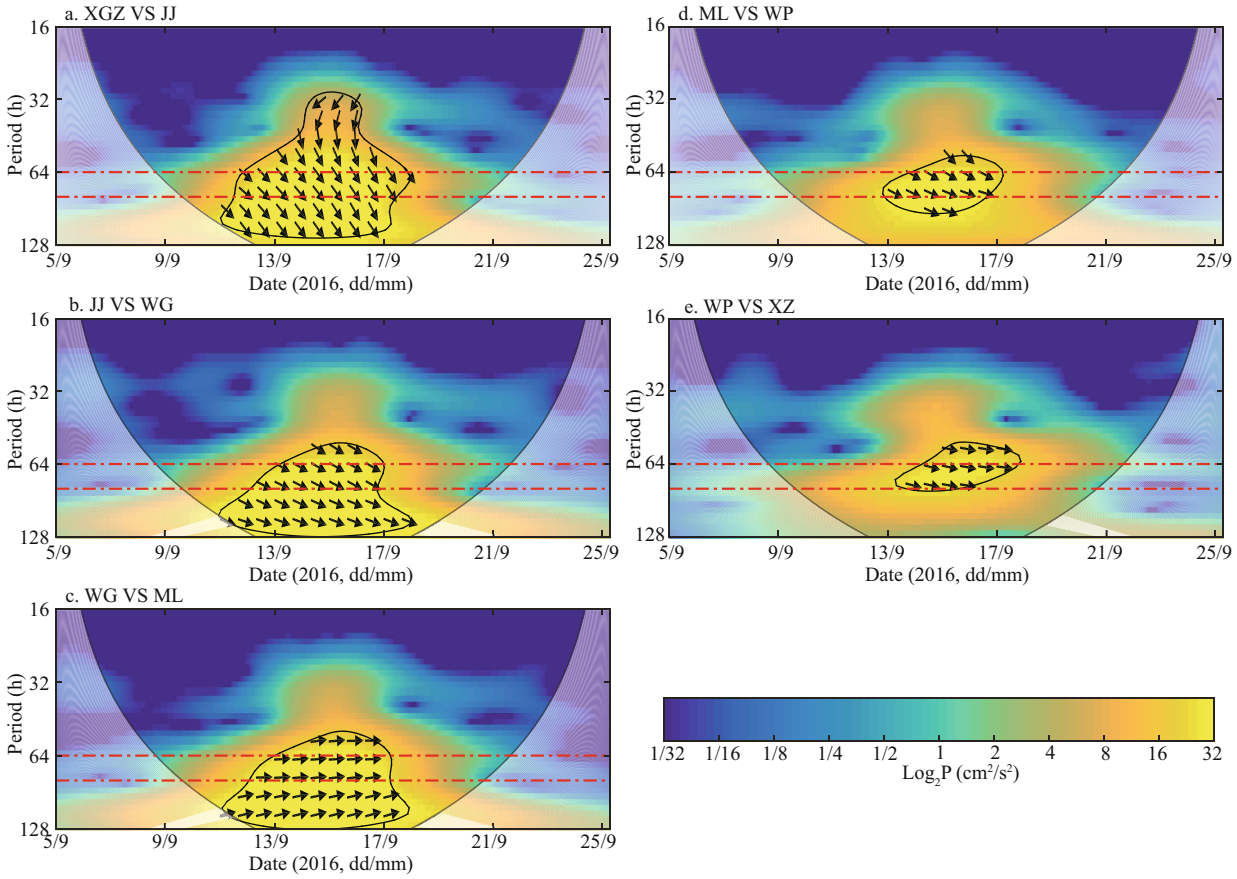

Fig.4 XWT of DSLA time series at tidal gauge station pairs (the thick line is the 5% significance level against red noise)

The relative phase relationship is also depicted in each panel with in-phase pointing to the right, anti-phase pointing to the left, and if the former would lead the latter by 90°, it will point straight downward. Red dash lines in each panel denote the period band of 64–81 h.

of satellite passing (15:22 UTC), the surge at JJ (which was about 25 km north of the inshore extent of Jason-2's ground track) was 0.30 m (Fig.2a). Without consideration of the above-mentioned large cross-shore sea surface slope near the coast, the small quantitative difference between altimetric estimate and tide-gauge data indicates the altimetry-observed storm surge magnitude was reliable.

In order to extract the CSW structure from the along-track SLA data acquired by satellite altimeter, the following assumptions are made:

(1) according to the result of Section 3.1, the scale of CSW along the coast was more than 1 500 km ($\lambda=c\times T$), which was obviously larger than the continental shelf width (~50 km) of Taiwan, China; hence, the satellite track is considered to be perpendicular to the coastline.

(2) the background field is derived from the gridded monthly mean SLA, and is used to remove trend of the along-track SLA (Fig.6b).

(3) set the origin of the coordinate system on the coastline, and the cross-shore axis positive seaward.

In the study area, we have the deep ocean depth

Table 2 Results of the XWT of the DSLA time series for different pairs of station

Station pair	Separation (km)	Phase angle and circular standard deviation (rad)	Lag (h)	Phase speed (m/s)
XGZ-JJ	153.8	0.76±0.09	8.8±1.0	4.9±0.6
XGZ-WG	189.5	1.15±0.12	13.2±1.4	4.0±0.4
XGZ-ML	219.3	1.11±0.09	12.8±1.1	4.8±0.4
XGZ-WP	333.4	1.45±0.10	16.6±1.1	5.6±0.4
XGZ-XZ	360.0	1.60±0.10	18.4±1.1	5.4±0.3
JJ-WG	35.7	0.39±0.02	4.5±0.2	2.2±0.1
JJ-ML	65.5	0.33±0.02	3.8±0.2	4.7±0.3
JJ-WP	179.6	0.69±0.06	7.9±0.7	6.3±0.6
JJ-XZ	206.2	0.85±0.10	9.8±1.1	5.9±0.7
WG-ML	29.7	-0.06±0.03	-0.7±0.3	-12.6±5.8
WG-WP	143.9	0.29±0.07	3.3±0.8	12.1±2.8
WG-XZ	170.4	0.45±0.12	5.2±1.3	9.2±2.4
ML-WP	114.2	0.35±0.05	4.0±0.6	7.9±1.2
ML-XZ	140.7	0.51±0.10	5.8±1.2	6.7±1.3
WP-XZ	26.5	0.15±0.05	1.8±0.6	4.2±1.3

The lag with a positive value indicates that the second station of the pair leads the first one. Phase speed (c) with a positive value indicates that the wave phase propagates alongshore with the coastline on its right side.

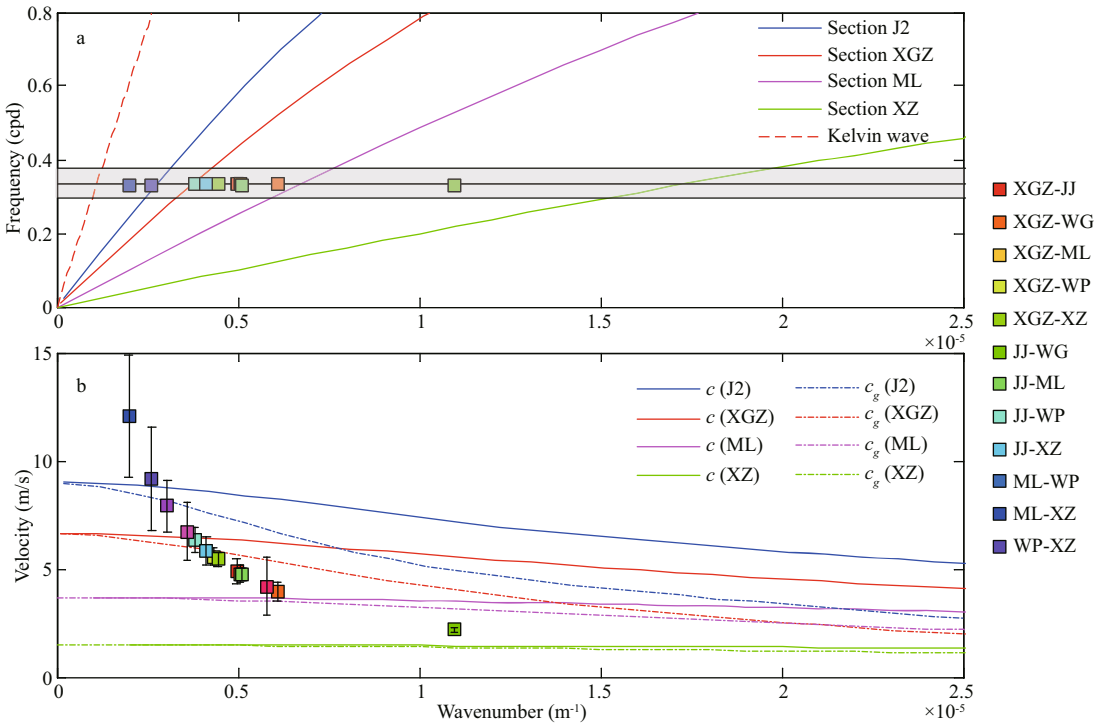

Fig.5 Dispersion relations for the first mode of the CSW for the sections depicted in Fig.1a. The black lines are the center frequency (0.33 cpd) with the period band of 64–81 h (denoted by the shaded region); the phase speed *c* (solid lines, *c*=*w*/*k* where *w* is frequency and *k* is wavenumber) and group speed c_g (dashed lines, c_g=d*w*/d*k*) are derived from the dispersion curves (b)

Squares in panel a and squares with error-bars in panel b are the data calculated from XWT; further, for a more direct comparison with theoretical expectations and the observational results, the observed relations between frequency and phase speeds are shown in panel b.

D=3 000 m, the continental shelf width l=47 km, the maximum shelf depth $\gamma \times D$=516 m, the Coriolis parameter f=5.6×10^{-5} s^{-1} and the gravitational acceleration g=9.8 m/s^2. Using these parameters, there will be an infinite number of roots μ_i specified for Eq.4. Hence, to solve the Eq.4, the zero-finding function in Matlab is applied, and the first three modes are listed in Table 3.

From Eq.5, the cross-shore structures of the first three CSW modes are derived, and the result is shown in Fig.7a. One can easily learn that Mode 1 decays exponentially across the shelf with the maximum amplitude locating at the shore, and reaches zero beyond the shelf. Moreover, Modes 2 and 3 show mostly the same maxima at the shore and near zero beyond the shelf; nevertheless, more complex structures on the shelf than that of Mode 1 are presented, which have two and three nodes on the shelf.

As shown in Fig.7b, the cross-shore SLA observed by satellite altimeter and the fitting result by using the first three theoretical CSW modes is depicted, while the corresponding fitting parameters are listed in Table 3. Obviously, the theoretical modes explain the cross-shore structure of CSW very well when we use the fitting goodness R^2 (up to 0.99) to describe how well the theoretical modes fit the observation. Moreover, the amplitude of the first mode is 0.20 m, and the amplitudes of the other two modes are 0.02 and 0.06 m, respectively, implying that the lowest (first) mode is the most dominant one.

Last but not least, one may doubt about the accuracy of altimeter data used in the study region. As noted by Roblou et al. (2011) due to land contamination, the application of satellite altimeter data over the continental shelf is still a challenging problem. The SLA accuracy in the open ocean is about 0.03 m for Jason-2, and decreases to 0.05 m in the coastal water (Birkett et al., 2011). Using the echo type of the return signal, Yang et al. (2011) evaluated land contamination on SLA accuracy, and he suggests that the distance of land effect on altimetry waveform is around 10 km. To minimize the land effect on the observation error of SLA in Fig.6b, the data beyond 10 km (about 11 km) from the coastline has been singled out for this study, where the accuracy of the altimeter data should be better than 0.05 m. The altimetry-observed storm surge and the CSW mode

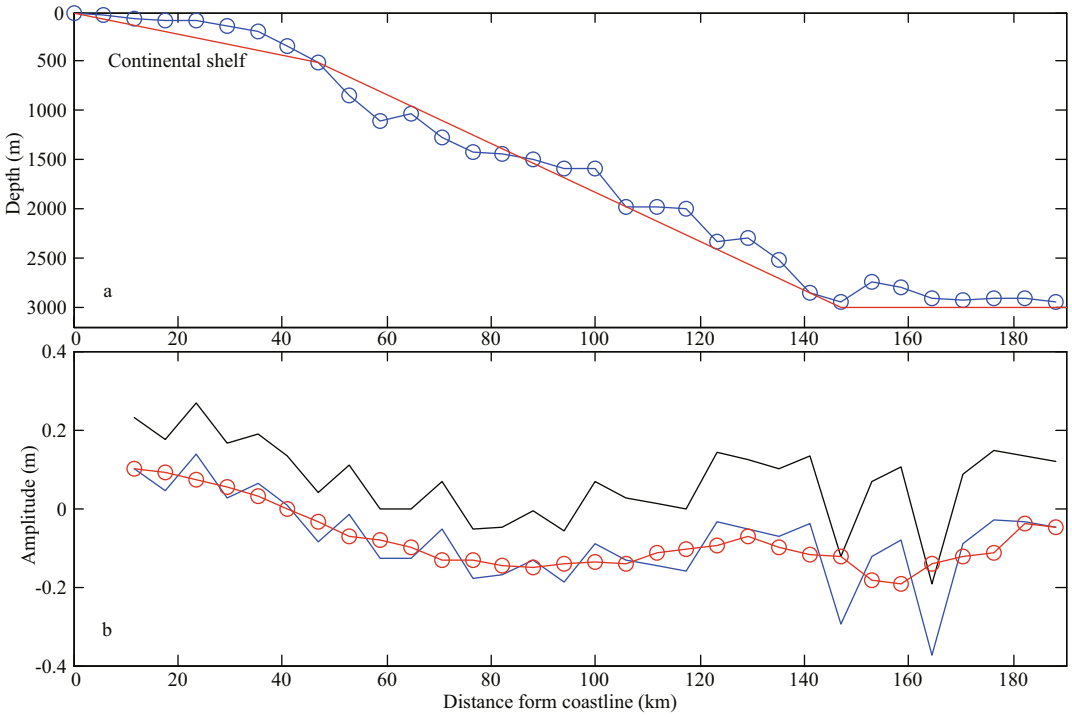

Fig.6 Mean cross-shore bathymetric profile (blue dotted line), and an idealized depth profile (red line) (a); SLA relative to the CLS01 mean topography along a track across Taiwan, China, observed by Jason-2 (b)

The satellite passing time during the impact of Meranti was around 15:22 UTC 14 September 2016. Raw data: black line; after removing background field with the period of 30 d: blue line; and 5-point moving average: red dotted line.

decomposition results in this study are statistically sound as the storm surge magnitude at the location close to the coast and the amplitude of the first (lowest) mode CSW are much larger than 0.05 m.

4 SUMMARY AND DISCUSSION

In this paper, we present the first study of the free barotropic CSW propagating in the eastern TWS using tidal gauge data and the along-track satellite altimeter data. This CSW event was characterized with strong barotropic response of coastal sea level within the range of 0.30–0.54 m during the passage of Typhoon Meranti in 2016. Particularly, through wavelet and cross-wavelet analyses on tidal gauge data, the CSW (with the period bands of 64–81 h) is shown to propagate along the east side of the TWS with the group and phase speeds up to 3 and 5.6± 0.7 m/s, respectively. Further, the group speed and phase speed were consistent with the dispersion curves for CSW with the first-mode derived from the four cross-shelf sections of the eastern TWS. Moreover, the Jason-2 satellite altimeter captured an along-track SLA before this CSW entered into the TWS. And a large cross-shelf slope was observed with the peak of storm surge magnitude of around 0.23–0.27 m locating at the coast area. Also, the theoretical cross-shore CSW modes are used to fit the along-track SLA data, and the results suggest that the first three wave modes can interpret this CSW event appeared in the southern TWS very well and the first-mode CSW (with an amplitude of 0.20 m) plays a dominant role.

Table 3 The first three modes for μ and the amplitude (A_i) for the first three CSW modes

Parameter	Mode 1	Mode 3	Mode 3
μ (s/m)	1.64	7.82	18.93
A_i (m)	0.20	0.02	0.06

However, the modes of this CSW event are not invariable. Indeed, the continuous change of the continental shelf will directly cause the transfer of energy between different modes. When the shelf width increases upward in the direction of wave propagation, the energy will change from low mode to high mode (Wilkin and Chapman, 1990), and the energy may be lost when passing through the headland, submarine canyon or the narrow shelf (Platov, 2016). In our case, this CSW event is still evident when it travels through the Penghu channel and enters into the TWS, the variable bathymetry will

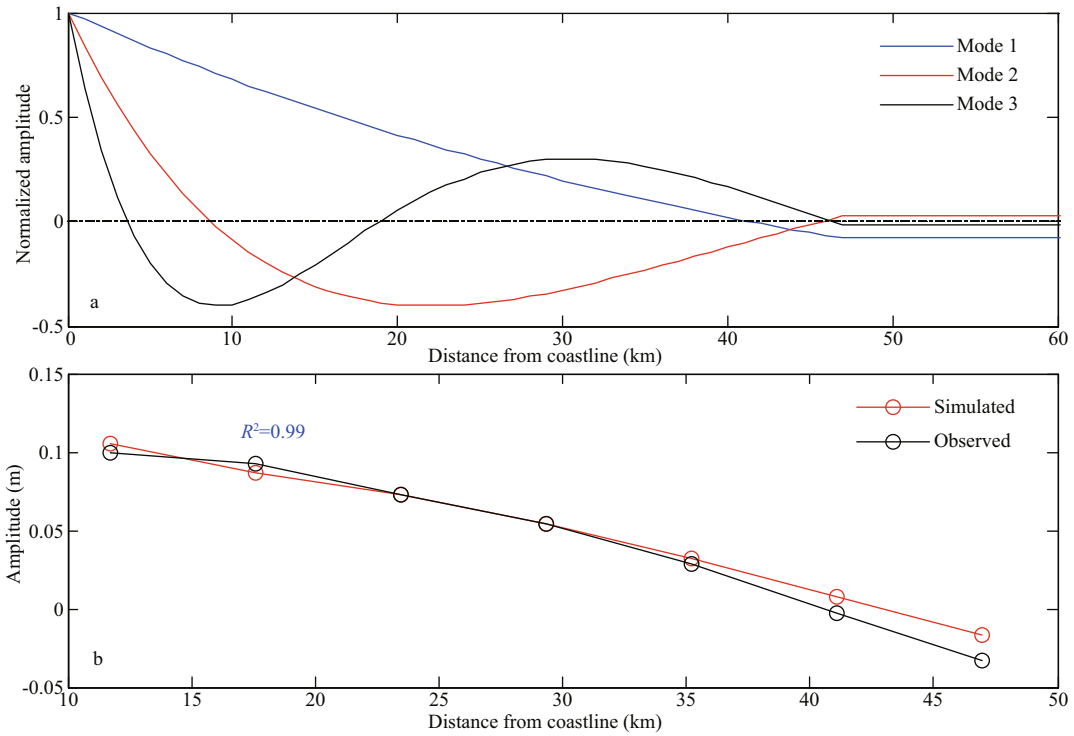

Fig.7 Normalized amplitudes of the first three theoretical CSW modes with the cross-shore component for idealized section depicted in Fig.6a (a); fitting along-track SLA data (black dotted curve) using the first three theoretical cross-shore CSW modes (red dotted curve) (b)

inevitably affect the CSW model. However, this statement is not conclusive, and numerical modeling studies are needed to understand effect of topography of TWS on changing the properties of CSW.

5 DATA AVAILABILITY STATEMENT

Data are available on request from the authors.

6 ACKNOWLEDGMENT

We thank the officers and crew of the mooring cruises for their support. We are grateful to the following organizations for providing their valuable data sets. Tidal gauge data are obtained from the website of the Central Weather Bureau of Taiwan, Taiwan (China) (http://www.cwb.gov.tw/). Satellite altimeter along-track SLA data are provided by the Center National d'Etudes Spatiales of France (www.aviso.altimetry.fr). The ERA-5 wind stress field is from the European Centre for Medium-Range Weather Forecasts (https://cds.climate.copernicus.eu). The typhoon track is obtained from the Regional Specialized Meteorological Center of Japan (http://www.jma.go.jp/jma).

References

Birkett C, Reynolds C, Beckley B, Doorn B. 2011. From research to operations: the USDA global reservoir and lake monitor. *In*: Vignudelli S, Kostianoy A G, Cipollini P, Benveniste J eds. Coastal Altimetry. Springer, Berlin Heidelberg. p.19-50.

Brink K H, Chapman D C. 1985. Programs for computing properties of coastal-trapped waves and wind-driven motions over the continental shelf and slope. Woods Hole Oceanographic Institution, Massachusetts.

Chen N, Han G Q, Yang J S, Chen D K. 2014. Hurricane Sandy storm surges observed by HY-2A satellite altimetry and tide gauges. *J. Geophys. Res. Oceans*, **119**(7): 4 542-4 548.

Chung S W, Jan S, Liu K K. 2001. Nutrient fluxes through the Taiwan Strait in spring and summer 1999. *J. Oceanogr.*, **57**(1): 47-53.

Ding Y, Bao X W, Shi M C. 2012. Characteristics of coastal trapped waves along the northern coast of the South China Sea during year 1990. *Ocean Dyn.*, **62**(9): 1 259-1 285.

Ding Y, Yu H M, Bao X W, Kuang L, Wang C X, Wang W J. 2011. Numerical study of the barotropic responses to a rapidly moving typhoon in the East China Sea. *Ocean Dyn.*, **61**(9): 1 237-1 259.

Grinsted A, Moore J C, Jevrejeva S. 2004. Application of the cross wavelet transform and wavelet coherence to geophysical time series. *Nonlin. Processes Geophys.*, **11**(5-6): 561-566.

Han G Q, Ma Z M, Chen D K, deYoung B, Chen N. 2012. Observing storm surges from space: hurricane Igor off Newfoundland. *Sci. Rep.*, **2**(1): 1 010.

Jordi A, Orfila A, Basterretxea G, Tintoré J. 2005. Coastal

trapped waves in the northwestern Mediterranean. *Cont. Shelf Res*., **25**(2): 185-196.

Kishimoto K, Inoue H, Hamada M, Shibuya T. 1995. Time frequency analysis of dispersive waves by means of wavelet transform. *J. Appl. Mech*., **62**(4): 841-846.

Lee Gordon R L, Huthnance J M. 1987. Storm-driven continental shelf waves over the Scottish continental shelf. *Cont. Shelf Res*., **7**(9): 1 015-1 048.

Li J Y, Zheng Q A, Hu J Y, Xie L L, Zhu J, Fan Z H. 2016. A case study of winter storm-induced continental shelf waves in the northern South China Sea in winter 2009. *Cont. Shelf Res*., **125**: 127-135.

Meyers S D, Kelly B G, O'Brien J J. 1993. An introduction to wavelet analysis in oceanography and meteorology: with application to the dispersion of Yanai waves. *Mon. Wea. Rev*., **121**(10): 2 858-2 866.

Park H C, Kim D S. 2001. Evaluation of the dispersive phase and group velocities using harmonic wavelet transform. *NDT E Int*., **34**(7): 457-467.

Pawlowicz R, Beardsley B, Lentz S. 2002. Classical tidal harmonic analysis including error estimates in MATLAB using T_TIDE. *Comput. Geosci*., **28**(8): 929-937.

Pedlosky J. 1987. Geophysical Fluid Dynamics. Springer-Verlag, New York and Berlin. p.628-636.

Platov G A. 2016. The influence of shelf zone topography and coastline geometry on coastal trapped waves. *Numer. Anal. Appl*., **9**(3): 231-245.

Price J F. 1981. Upper ocean response to a hurricane. *J. Phys. Oceanogr*., **11**(2): 153-175.

Roblou L, Lamouroux J, Bouffard J, Lyard F, Le Hénaff M, Lombard A, Marsaleix P, De Mey P, Birol F. 2011. Post-processing altimeter data towards coastal applications and integration into coastal models. *In*: Vignudelli S, Kostianoy A G, Cipollini P, Benveniste J eds. Coastal Altimetry. Springer, Berlin Heidelberg. p.217-246.

Sanford T B, Black P G, Haustein J R, Feeney J W, Forristall G Z, Price J F. 1987. Ocean response to a hurricane. Part I: observations. *J. Phys. Oceanogr*., **17**(11): 2 065-2 083.

Schulz W J Jr, Mied R P, Snow C M. 2012. Continental shelf wave propagation in the Mid-Atlantic Bight: a general dispersion relation. *J. Phys. Oceanogr*., **42**(4): 558-568.

Shen J Q, Qiu Y, Zhang S W, Kuang F F. 2017. Observation of tropical cyclone-induced shallow water currents in Taiwan strait. *J. Geophys. Res. Oceans*, **122**(6): 5 005-5 021, https://doi.org/10.1002/2017JC012737.

Tang C L, Gui Q, DeTracey B M. 1998. Barotropic response of the Labrador/Newfoundland shelf to a moving storm. *J. Phys. Oceanogr*., **28**(6): 1 152-1 172.

Thiebaut S, Vennell R. 2010. Observation of a fast continental shelf wave generated by a storm impacting Newfoundland using wavelet and cross-wavelet analyses. *J. Phys. Oceanogr*., **40**(2): 417-428.

Torrence C, Compo G P. 1998. A practical guide to wavelet analysis. *Bull. Amer. Meteor. Soc*., **79**(1): 61-78.

Wilkin J L, Chapman D C. 1990. Scattering of coastal-trapped waves by irregularities in coastline and topography. *J. Phys. Oceanogr*., **20**(3): 396-421.

Yang L, Lin M, Zhang Y, Bao L, Pan D. 2011. Evaluation of Retracking algorithms over china and adjacent coastal seas. *In*: Vignudelli S, Kostianoy A G, Cipollini P, Benveniste J eds. Coastal Altimetry. Springer, Berlin Heidelberg. p.453-471.

Zar J H. 1999. Biostatistical Analysis. 4th edn. Prentice-Hall, Upper Saddle River, N.J. p.931.